Modeling Global Electron Precipitation Driven by Whistler Mode Waves: Integrating Physical and Deep Learning Approaches

Sheng Huang[1], Wen Li[1], Qianli Ma[1,2], Xiao-Chen Shen[1], Luisa Capannolo[1] and Xiangning Chu[3]

[1]Center for Space Physics, Boston University, Boston, MA, USA.

[2]Department of Atmospheric and Oceanic Sciences, University of California, Los Angeles, CA, USA.

[3]Laboratory for Atmospheric and Space Physics, University of Colorado Boulder, Boulder, CO, USA.

Corresponding author: Sheng Huang (hs2015@bu.edu); Wen Li (wenli77@bu.edu)

Key Points:

- We integrate physical and deep learning approaches to simulate electron precipitation due to whistler mode waves in a storm event
- The simulation captures the dynamics of the electron precipitation observed by POES throughout the storm period
- Electron precipitation is primarily driven by chorus waves during the main phase, but plume hiss becomes important in the recovery phase

Abstract

Whistler mode waves scatter energetic electrons, causing them to precipitate into the Earth's atmosphere. While the interactions between whistler mode waves and electrons are well understood, the global distribution of electron precipitation driven by whistler mode waves needs futher investigations. We present a two-stage method, integrating neural networks and quasi-linear theory, to simulate global electron precipitation driven by whistler mode waves. By applying this approach to the 17 March 2013 geomagnetic storm event, we reproduce the rapidly varying precipitation pattern over various phases of the storm. Then we validate our simulation results with POES/MetOp satellite observations. The precipitation pattern is consistent between simulations and observations, suggesting that most of the observed electron precipitation can be attributed to scattering by whistler mode waves. Our results indicate that chorus waves drive electron precipitation over the premidnight-to-afternoon sector during the storm main phase, with simulated peak energy fluxes of 20 erg/cm^2/s and characteristic energies of 10-50 keV. During the recovery phase, plume hiss in the afternoon sector can have a comparable or stronger effect than chorus, with peak fluxes of ~1 erg/cm^2/s and characteristic energies between 10 and 200 keV. This study highlights the importance of integrating physics-based and deep learning approaches to model the complex dynamics of electron precipitation driven by whistler mode waves.

Plain Language Summary

Whistler mode hiss and chorus waves are electromagnetic waves in Earth's magnetosphere that interact with electrons, altering their motion and causing them to precipitate into the atmosphere. Understanding electron evolution is crucial, as precipitating electrons affect ionospheric conductivity and atmospheric chemistry, leading to aurorae and other phenomena. However, direct observations of electron precipitation caused by these waves are scarce, and global simulations are challenging due to the dynamic nature of wave-particle interactions. This study presents a two-stage simulation framework that models global wave activities using deep learning and runs physics-based simulations with the neural network output as inputs. We validate our results by comparing them with the multi-point POES/MetOp observations during a geomagnetic storm event on 17 March 2013, successfully reproducing the dynamic evolution of the observed precipitation. We found that chorus waves predominantly drive energetic electron precipitation during the storm main phase, while plume hiss causes comparable or stronger precipitation during the recovery phase. Our study highlights the importance of whistler mode waves in electron precipitation, identifies the quantitative contribution of hiss and chorus waves at different storm phases, and demonstrates how deep learning can advance scientific research in understanding the complex dynamics of electron precipitation in Earth's magnetosphere.

1. Introduction

Whistler mode waves are right-hand polarized electromagnetic emissions with frequencies below the electron cyclotron frequency (Stix, 1992). Through pitch angle diffusion, whistler mode waves scatter radiation belt electrons, leading to electron precipitation into Earth's atmosphere (Abel & Thorne, 1998; Millan & Thorne, 2007; Thorne et al., 2021). Among them, hiss waves are broadband emissions primarily confined to high-density regions, including the plasmasphere and plumes. Hiss waves significantly contribute to the decay of energetic electrons ranging from tens of keV to 1 MeV in the outer radiation belt during both quiet and geomagnetically disturbed periods (Lam et al., 2007; Ma et al., 2015, 2016; Meredith et al.,

2006) and are responsible for the formation of the slot region (Lyons et al., 1972; Meredith et al., 2007, 2009). In the plasma trough, whistler mode chorus waves are observed over the night-dawn-noon sector along the electron drift path (Li et al., 2009, 2011; Meredith et al., 2001, 2012), and are excited by anisotropic electron distributions injected from the magnetotail (Fu et al., 2014; Li et al., 2008; Su et al., 2014). Chorus waves are considered as an important driver of electron precipitation, especially at energies ranging from a few to hundreds of keV, in the outer radiation belt (Ni et al., 2008; Hikishima et al., 2010; Ma et al., 2012), leading to the formation of diffuse and pulsating aurora (Kasahara et al., 2018; Ni et al., 2014; Nishimura et al., 2010, 2013; Thorne et al., 2010).

Recent studies have linked signatures of electron precipitation with whistler mode waves. Qin et al. (2021) identified a high temporal correlation between whistler mode waves and precipitating electrons from multi-point observations. Breneman et al. (2015) provided evidence of radiation belt electron loss caused by hiss, with a spatial scale comparable to the plasmasphere, suggesting a general role of hiss waves in driving electron precipitation. Statistical studies indicate that the precipitating electron flux increases with geomagnetic activity, peaking during active conditions outside of the plasmapause on the dawnside (Lam et al., 2010), consistent with the evolution of chorus waves. However, direct observations of precipitating electron flux driven by whistler mode waves are very limited. As illustrated in Figure 1a, electron precipitation into the Earth's atmosphere can be detected by Low-Earth-Orbiting (LEO) satellites, while plasma waves are typically observed by high-altitude satellites near the equatorial plane. Thus, conjunction events are rare and have only been examined in a small number of case studies (e.g., Li et al., 2019; Shen et al., 2023).

To estimate the global effect of whistler mode waves on electron precipitation, statistical methods have been developed. Ma et al. (2020, 2021) conducted global surveys of electron precipitation and indicated that during disturbed times (AE > 500 nT), chorus waves precipitate 3-10 erg/cm^2/s energy flux with characteristic energy mostly around 10-20 keV on the dawn side, while hiss waves precipitate 0.3-1 erg/cm^2/s energy flux with characteristic energy from tens of keV to ~100 keV on the dusk side, with plume hiss being more effective in driving electron precipitation than plasmaspheric hiss. However, the global maps of electron precipitation patterns and precipitating energy flux levels are averaged over a long period and cannot reproduce storm-time dynamics on a short time scale when the wave evolution is highly dynamic and/or very intense precipitation occurs (Chakraborty et al., 2021; Zhu et al., 2018). Furthermore, Reidy et al. (2021) conducted MLT-dependent electron precipitation simulations due to statistically derived chorus and hiss waves and compared results with the POES observations. They found that the best agreement occurs at L^*>5 on the dawnside in the >30 keV electron channel, which is consistent with the precipitation driven by lower band chorus. However, additional mechanisms are needed to explain the flux at higher energies and on the dusk side. Therefore, a more realistic wave and electron density model is required to simulate global electron precipitation with higher spatial and temporal resolution and understand the relative contributions from various types of whistler mode waves under different storm phases.

In recent years, machine learning techniques have been applied to study the dynamics of the inner magnetosphere, including plasma density (Bortnik et al., 2016; Chu et al., 2017a,b; Huang et al., 2022; Zhelavskaya et al., 2017), chorus and hiss waves (Bortnik et al., 2018; Chu et al., 2023, 2024; Huang et al., 2023), and electron fluxes (Chu et al., 2021; Ma et al., 2023, 2024), demonstrating their advantages over statistical methods. Huang et al. (2022) showed that with a deep learning approach, the evolution of electron density and the formation of a dayside plume can be well reproduced. Such dynamics are key to facilitate electron precipitation through wave-particle interactions (Breneman et al., 2015). The simulations conducted by Huang et al. (2023), which adopted hiss wave distributions based on a deep learning model, reproduced the fast decay of energetic electrons in the storm main phase, demonstrating the potential of combining deep learning techniques with physics-based simulations to improve accuracy. In the present study, we propose a new framework integrating deep learning with quasi-linear diffusion theory to model the global electron precipitation induced by whistler mode waves. The simulation methodology for electron precipitation, which includes both the deep learning model and physics-based simulation, is described in Section 2. In Section 3, we present the observations of electron precipitation during the March 17, 2013 storm. The simulation results of electron precipitation on a global scale, as well as their comparison to the observations, are shown in Section 4. Finally, we summarize our principal findings in Section 5.

2. Simulation Methodology of Electron Precipitation

2.1 Deep Learning Model of Density, Waves, and Trapped Electron Flux

To perform a global simulation of electron precipitation driven by whistler mode waves (Figure 1a), we first train the neural network on electron density, whistler mode wave amplitude, and electron fluxes from the 7-year observations by Van Allen Probes (RBSP) (Mauk et al., 2013; VAP, 2013a, 2013b). Electron density is inferred from the upper hybrid resonance frequency from the High Frequency Receiver (HFR) measurement (Kurth et al., 2015). Waves are measured by the Waveform Receiver (WFR) of the Electric and Magnetic Field Instrument Suite and Integrated Science (EMFISIS) instrument (Kletzing et al., 2013). Whistler mode hiss (chorus) waves were selected with the following criteria (Li et al., 2015; Shen et al., 2019): a) inside (outside) plasmasphere based on the ECH wave power (Shen et al., 2019), b) wave ellipticity >0.7 (>0.7), c) wave planarity >0.2 (>0.6), d) spectral frequency range between 20–4000 Hz (0.05-0.8 electron cyclotron frequency). Hiss and chorus wave amplitudes are calculated by integrating their magnetic wave power over the corresponding frequency ranges. Electron fluxes at energies of 1 keV – 1 MeV were obtained from the electron flux measurements at pitch angles of ~18° by HOPE (Funsten et al., 2013) and ~24.5° by MagEIS (Blake et al., 2013) from the Energetic Particle Composition and Thermal Plasma (ECT) suite (Spence et al., 2013), as an estimate of the fluxes just outside the loss cone (Ma et al., 2020). These electron fluxes were interpolated into 30 energy channels evenly distributed on a logarithmic scale. All data were averaged per minute and normalized before training.

As shown in Figure 1b, we developed a primary and an auxiliary model. The auxiliary model (Figure 1b bottom) is an autoencoder of several fully-connected neural network layers, useful for data compression (e.g., Wang et al., 2014) and reducing the dimensionality of the electron flux from 30 energy channels to a dimension of 5. The auxiliary model limits the data size of the trapped electron flux in the primary model training while preserving the energy profile measured by RBSP. This method is preferred over simple linear interpolation which limits the information content of the entire energy spectrum. The primary deep learning model (Figure 1b top) follows Huang et al. (2023), where the history of geomagnetic indices (SYM-H, SMU, SML, and Hp30; Gjerloev, 2012; Matzka et al., 2022; Papitashvili et al., 2020) and the satellite location are processed with an encoder-decoder architecture to provide maps of electron density, hiss wave amplitude, chorus wave amplitude, and compressed electron flux. The model structure is organized as follows: a Long Short-Term Memory (LSTM; Hochreiter & Schmidhuber, 1997) neural network takes the historical geomagnetic indices as inputs and compresses the information into a vector, which represents the inner magnetospheric state at the current time; the extracted information, together with the satellite location, is processed by another fully connected neural network to estimate the distribution of the parameter (mean and standard deviation) at a given location; according to the distribution, a final output is randomly sampled, representing the uncertainty in both data and model.

We train one model for the density and the whistler mode waves, and another model for the electron flux in the 5 compressed energy channels. After the models are trained, we predict the global distribution of the parameters by applying models to an artificial spatial grid which covers the whole equatorial plane (with 0.2 L and 0.5 MLT resolution). We advance the prediction every 1 minute to obtain the global evolution of the parameters. To obtain the electron flux from the modeled compressed flux, we apply the trained decoder in the auxiliary model to recover the 30 original electron channels that will be used for the following simulation (Figure 1c and Section 2.2). Detailed configurations of the neural networks and the neural network model performance can be found in the Supporting Information (Text S1-S2, Figures S1–S3).

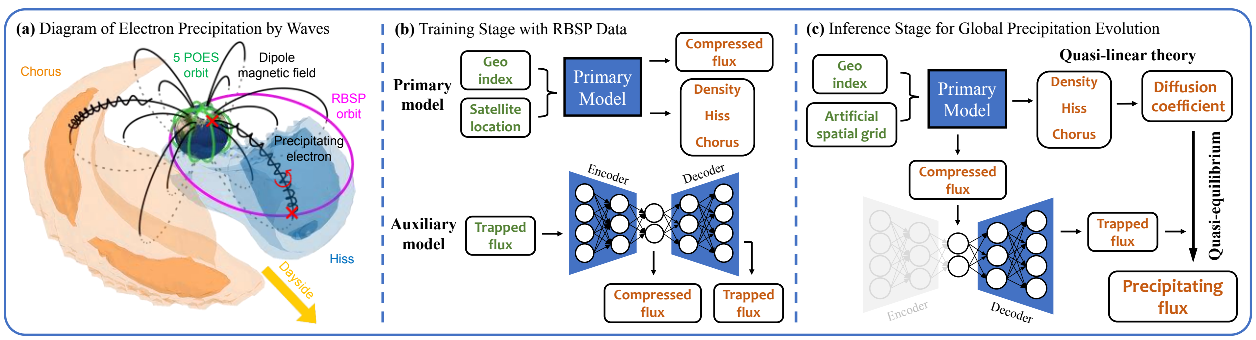

Figure 1. Overview of the 2-stage method for simulating electron precipitation. (a) Diagram of electron precipitation driven by whistler mode waves (chorus and hiss) and orbits of POES (green) and RBSP (pink) satellites. (b) Workflow for training neural networks of electron density, hiss, chorus, and trapped flux. (c) Simulation process of global electron precipitation using trained neural network models.

2.2 Quasilinear Modeling of Electron Precipitation Driven by Whistler Mode Waves

After the neural network models are trained, we perform simulations to calculate the global electron precipitation flux, as shown in Figure 1c. The maps of electron density, hiss wave amplitude, chorus wave amplitude, and compressed trapped flux are obtained by applying the trained neural networks on an artificial spatial grid that covers L-shells from 1.2 to 6.6 and all magnetic local times (MLT), with resolution of 0.2 L and 0.5 MLT. The electron density and amplitude of chorus and hiss waves are used as inputs to the Full Diffusion Code based on quasi-lineary theory (Ma et al., 2018; Ni et al., 2008) to calculate the electron pitch angle diffusion coefficients due to chorus and hiss waves. The Full Diffusion Code also requires information on the wave spectra and wave normal angle distribution. In the simulation, chorus and hiss wave frequency spectra were adopted based on the statistical results (Li et al., 2015, 2016). The latitudinal coverage of chorus waves is 0°-15° at 00-04 MLT, 0°-25° at 04-08 MLT, 0°-45° at 08-16 MLT, and 0°-20° at 16-24 MLT based on the statistical results (e.g., Meredith et al., 2012), assuming a constant wave magnetic field amplitude along the field line. The wave normal angle (θ) distribution of chorus wave magnetic power is assumed as a Gaussian distribution in $\tan\theta$, with central $\theta_m = 0°$, width $\theta_w = 30°$, minimum $\theta_{min} = 0°$, and maximum $\theta_{max} = 45°$. The hiss wave latitude range is 0°-45°, and the wave normal angles change from quasi-field-aligned near the magnetic equator to more oblique at higher latitudes following the latitudinally-varying model by Ni et al. (2013).

After the diffusion coefficients are calculated, we use the method of Ma et al. (2020, 2021) to calculate the electron flux inside the loss cone. The ratio between electron fluxes at a pitch angle near the center of the loss cone and outside the loss cone is

$$\chi(E) = \frac{2\int_0^1 I_0[Z_0(E)\tau]\cdot\tau\cdot d\tau}{I_0[Z_0(E)]} \tag{1}$$

$$Z_0(E) = \sqrt{D_{\mathrm{SD}}/\langle D_{\alpha\alpha}\rangle_{\mathrm{LC}}} \tag{2}$$

where E is electron kinetic energy, I_0 is the modified Bessel function, D_{SD} is the strong diffusion limit, and $\langle D_{\alpha\alpha}\rangle_{\mathrm{LC}}$ is the bounce-averaged pitch angle diffusion coefficient at the loss cone. We calculate the precipitating flux inside the loss cone (J_{prec}) as a function of time, L, MLT, and energy by multiplying the ratio $\chi(E)$ with modeled trapped electron flux just outside the loss cone. Using the energy profile of the precipitating electron flux, we calculate the characteristic precipitating energy E_c (keV)

$$E_{\mathrm{c}} = \frac{\int_{E_{\mathrm{min}}}^{E_{\mathrm{max}}} J_{\mathrm{prec}}\cdot E\cdot dE}{\int_{E_{\mathrm{min}}}^{E_{\mathrm{max}}} J_{\mathrm{prec}}\cdot dE} \tag{3}$$

and the total precipitating energy flux Q_{tot} (erg·cm^{-2}·s^{-1})

$$Q_{tot} = \pi\int_{E_{\mathrm{min}}}^{E_{\mathrm{max}}} J_{\mathrm{prec}}\cdot E\cdot dE \tag{4}$$

with an energy range between 1 keV and 1 MeV. The integral directional flux of precipitating electrons I_{tot} (cm^{-2}·s^{-1}sr^{-1}) for energies >30 keV is calculated as

$$I_{tot} = \int_{E_{\mathrm{min}}}^{E_{\mathrm{max}}} J_{\mathrm{prec}}\cdot dE \tag{5}$$

with $E_{\mathrm{min}} = 30\mathrm{keV}$ and $E_{\mathrm{max}} = 1\mathrm{MeV}$, to be consistent with the POES observations, as discussed in Section 4.

3. Electron Precipitation During a Storm Event

3.1 Electron Precipitation Observation by POES

We use data from the POES/MetOp constellation (POES, 2012), which consists of up to 7 LEO (~800-850 km of altitude) satellites that provide wide spatial coverage (Evans & Greer, 2004). Onboard each satellite, the Medium Energy Proton and Electron Detector (MEPED) measures electron flux in three integral channels (>30 keV, >100 keV, >300 keV) and proton flux in several differential channels (30–80 keV, 80–250 keV, and 250–800 keV), with two telescopes measuring predominantly precipitating flux (0°) and trapped flux (90°) (Rodger et al., 2010). In our analysis, we use the precipitating electron flux at the >30 keV energy channel (Green, 2013). As the POES electron channels are affected by proton contamination (Capannolo et al., 2019; Yando et al., 2011), we remove the periods of intense proton contamination when the 80–250 keV precipitating proton count rate exceeds 10^3/s (indicating strong proton precipitation) and is larger than the >30 keV precipitating electron count rate. While this method is not as sophisticated as existing ones (Peck et al., 2015; Pettit et al., 2021), it discards heavily contaminated events while preserving as much data as possible. In the following sections, we present results from all available POES satellites using this cleaned electron precipitating flux.

3.2 Overview of the 17 March 2013 Storm Event

Figure 2 presents a case study of electron precipitation during a storm event on 17 March 2013 with a minimum SYM-H index of -130 nT driven by a massive coronal mass ejection (Baker et al., 2014). Figures 2b-2e show the >30 keV electron precipitation flux observed by POES at different L-shells and MLTs. Before the storm onset, the inner magnetosphere was quiet with weak precipitation. After the storm onset at 06:00 UT on March 17, intense precipitation occurred over 21-09 MLT, especially at L >5, possibly caused by enhanced chorus waves. During the main phase (09-24 UT), enhanced electron precipitation was observed at all MLTs, extending to L ~3. Electron precipitation from 15 to 21 MLT is weaker than other MLTs. In the storm recovery phase on March 18, precipitation over 15-03 MLT persisted at higher L than at 03-15 MLT. Overall, the observed precipitation is highly dynamic, with varying intensities depending on L and MLT during different phases of the storm.

Figure 2f shows the integral electron flux at >30 keV energy observed by RBSP near midnight. We use differential fluxes averaged at pitch angles of 8° and 172° to estimate the upper limit of the precipitation flux. Electron density, hiss, and chorus wave amplitudes are shown in Figures 2g-2i for RBSP-A in blue and RBSP-B in orange for both satellite observations (darker solid line) and deep learning (primary) model predictions (lighter dashed line). At the beginning of the storm, electron density responded quickly, the plasmapause density gradient was sharpened (Figure 2g), and strong chorus waves (Figure 2i) were immediately excited. Increased precipitating flux at L >3 was observed during the storm main phase and the precipitation region moved to larger L shells during the recovery phase. In addition, chorus waves were intensified during the main phase, while the intensification of hiss wave activity was more evident in the recovery phase (Figure 2h). Overall, the deep learning model reproduced the observed dynamics of density, hiss and chorus wave amplitudes reasonably well.

The 17 March 2013 storm has been studied extensively, covering interplanetary drivers, electron acceleration by chorus waves (Li et al., 2014; Xiao et al., 2014; Ma et al., 2018), and ionospheric response (Lyons et al., 2016; Schunk et al., 2021). However, simulating the global evolution of electron loss relies heavily on the global wave distribution, which cannot be obtained from in-situ observations alone. In this event, RBSP was located on the nightside (21-03 MLT, Figure 2j), thus did not provide direct wave observations to explain the precipitation patterns observed by POES at other MLTs. Due to the lack of global wave observations, MLT-averaged wave parameters are usually adopted (Chen et al., 2019; Søraas et al., 2018), and thus it is difficult to estimate the MLT-dependent electron precipitation during different storm phases. In Section 4, we present our global simulation results and compare them to the POES observations.

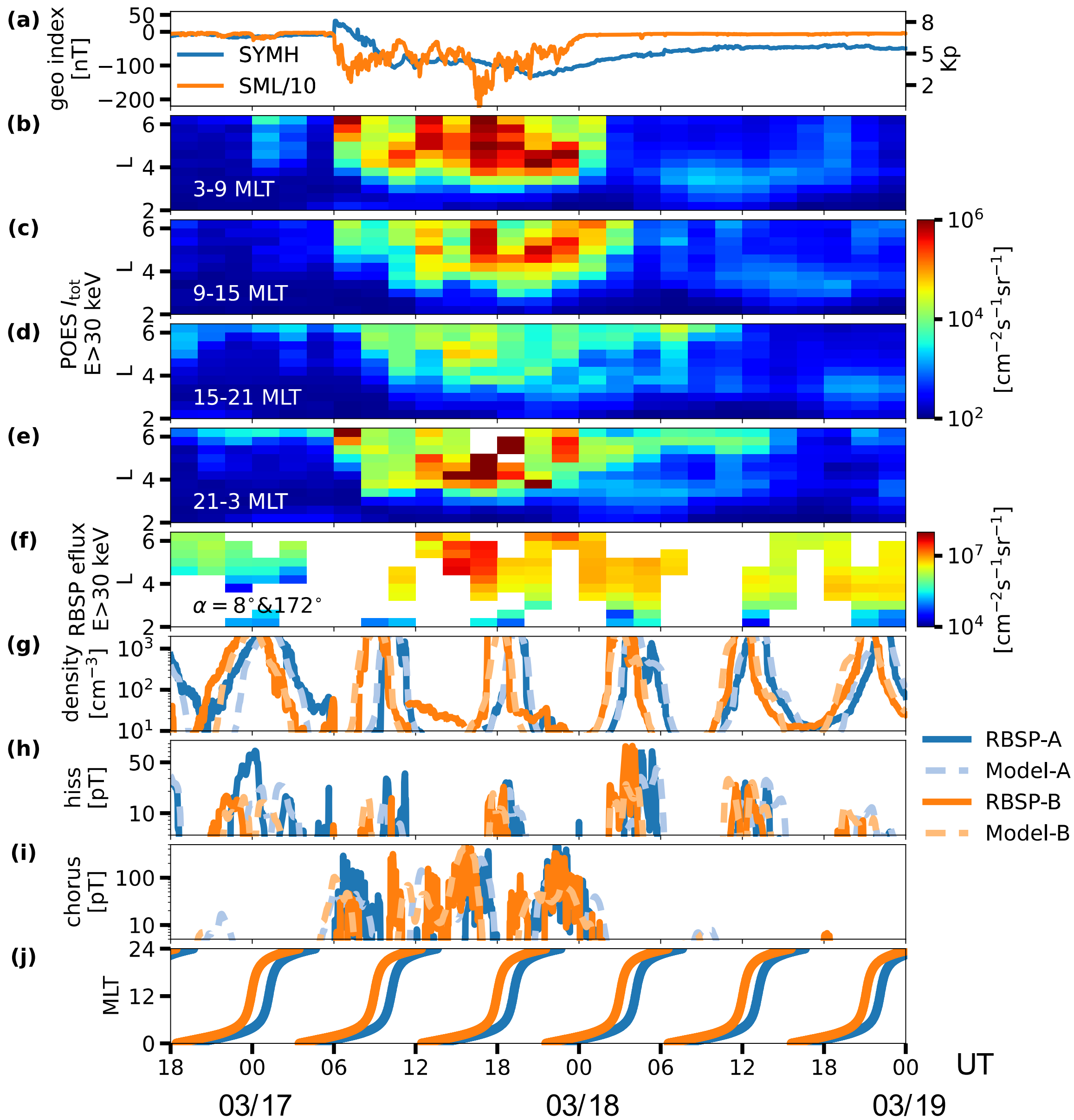

Figure 2. Overview of the 17 March 2013 geomagnetic storm. (a) Geomagnetic indices SYM-H, SML, and Kp. (b-e) Precipitating electron flux (>30 keV) observed by POES in different MLT ranges. (f) Integral electron flux (>30 keV) averaged at pitch angles of 8° and 172° observed by RBSP. (g-i) Electron density, hiss, and chorus wave amplitudes from RBSP observations (darker solid lines) and primary model predictions (lighter dashed lines) for RBSP-A (blue) and RBSP-B (orange).

4. Simulation Result

4.1 Simulated Global Evolution of Precipitating Electron Energy Flux

Figure 3 presents results from two simulations: Simulation 1 with deep learning density, hiss and chorus wave amplitudes as inputs (Figures 3b-3d), and Simulation 2 using statistical wave and density parameters as inputs (Figure 3e-3g). The statistical parameters are obtained from Model 4 (Ma et al., 2023), parameterized with Hp30* and SML. This model generally shows low error compared to RBSP observations but can exhibit large deviations near the dynamic plasmapause or in plumes. We use this recently developed model to represent the performance of simulations using statistical models as inputs in general. The simulation results on the equatorial plane are shown for Times 1-5, covering different storm phases. Figure 3b shows the whistler mode wave amplitude using the deep learning model, with the magenta circle representing the plasmapause location (30 cm^{-3} density contour), separating waves into hiss (inside) and chorus (outside). Figures 3c and 3d show the global evolution of simulated characteristic energy (E_c) and total precipitating energy flux (Q_{tot}) from Equations (3) and (4), respectively.

Before the storm, wave activity (Figure 3b1) was weak, with characteristic energies of ~40 keV for both hiss and chorus, and low electron flux precipitating into the atmosphere. At the storm onset (Time 2), coincident with injected electrons from the nightside, strong chorus waves were excited at L ≥ 4 over 0–12 MLT. As the convection electric field increased, a plasmaspheric plume was formed with intense plume hiss inside of it. The characteristic energy of precipitating electrons decreased to ~10 keV due to enhanced low-energy electron precipitation, and the peak precipitating energy flux increased to ~3 $erg/cm^2/s$ for chorus and ~1 $erg/cm^2/s$ for hiss, significantly higher than those during quiet times. In the storm main phase (Time 3), plume hiss quickly developed while chorus waves remained strong. Precipitation was thus dominated by chorus waves with peak Q_{tot} reaching 20 $erg/cm^2/s$ at 21-12 MLT. In the early recovery phase (Time 4), chorus waves dissipated rapidly. Remnants of plume hiss scattered electrons from 50 keV (L = 6) to 200 keV (L = 3.5), with Q_{tot} close to 1 $erg/cm^2/s$, comparable to chorus waves that scattered electrons from 20 keV (MLT=15) to 50 keV (MLT=0). At Time 5, the inner magnetosphere returned to a quiet state with weak wave activity at L > 4 and little precipitation driven by either wave mode.

Figures 3e-3g show Simulation 2 results based on the statistical distributions of density, hiss, and chorus, with trapped flux from the deep learning model. Overall, the simulation using statistical distributions presents a similar precipitation level to the simulation using the deep learning model (Simulation 1). However, before the storm the statistical results indicate a moderate level of wave activity (Figure 3e Time 1), while weak wave activity is expected during quiet times. Moreover, in the recovery phase, statistical results exhibit small variations in wave activity. Because Hp30* is higher than 6, the plasmasphere is compressed with moderate chorus waves persistent over the nightside-dawn-dayside sector for more than 20 hours after the storm main phase. In contrast, the deep learning model demonstrates the rotation of the plasmasphere and a quick response of the wave activity therein, with little chorus waves up to L=6.6. As a result, the Simulation 2 results exhibit less dynamics in electron precipitation as well as wave activity compared to Simulation 1 due to the difficulty of statistical models in resolving the spatial and temporal evolution of storm-time dynamics.

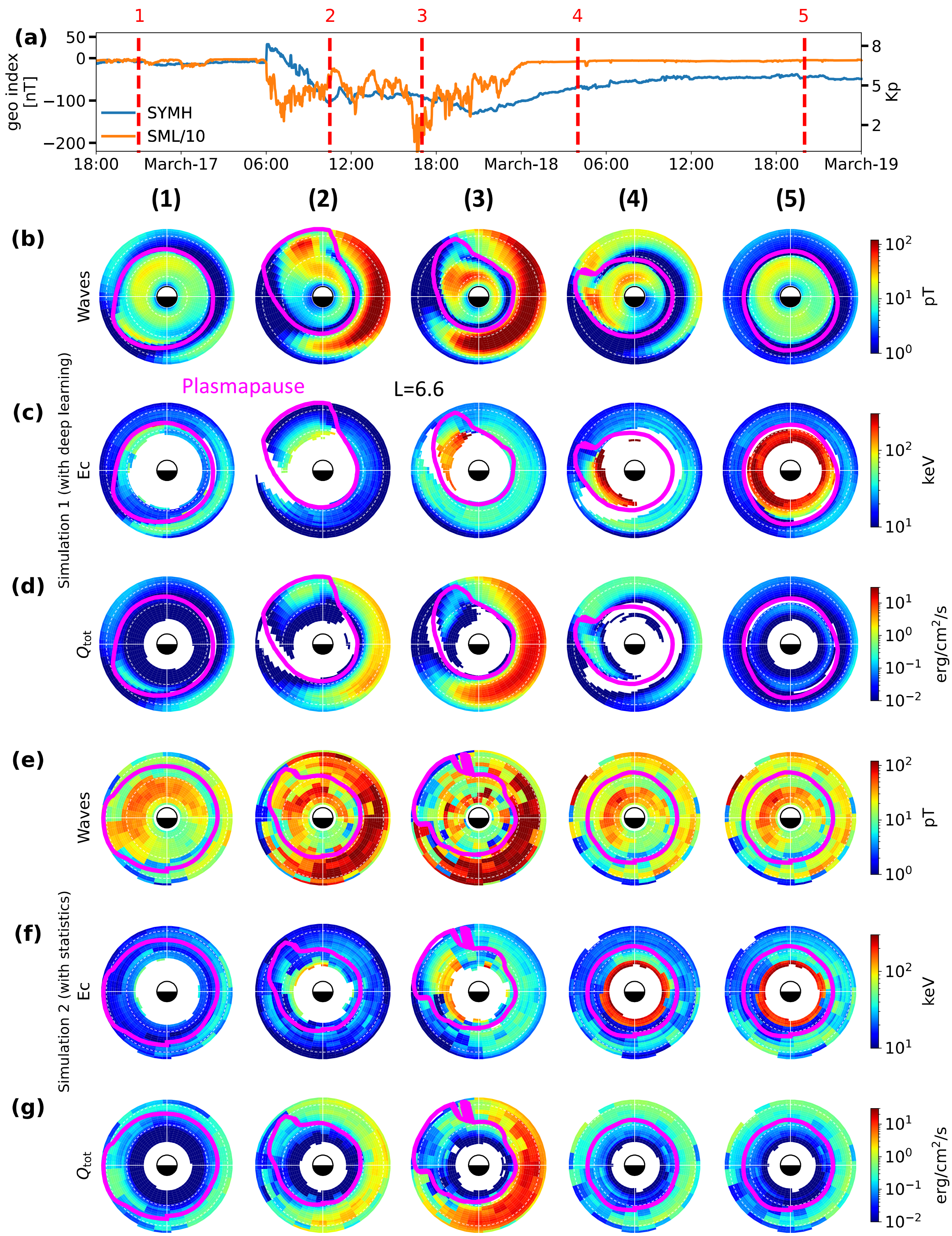

314

315 **Figure 3.** Snapshots of simulation results in the L-MLT coordinates. (a) Geomagnetic Sym-H,

SML, and Kp indices. (b) Whistler mode wave amplitudes based on the deep learning model at times marked in (a). Magenta line denotes the plasmapause location from the density model, separating hiss (inside) from chorus (outside). (c) Simulated characteristic energy of precipitating electrons. (d) Simulated electron precipitating energy flux. (e-g) Same as (b-d) but for simulation results using statistical models as inputs.

4.2 Comparison of Simulated and Observed Precipitating Electron Fluxes

We validate the simulation results by comparing them to the POES observations of precipitating electron flux (Figure 4). POES observations (Figure 4d) are binned in every 2 hours, 0.5 L, and 1 MLT to balance spatial coverage and resolution. Waves from the deep learning model are shown in Figure 4b, with the magenta line indicating the plasmapause location from the density model. The simulated precipitating electron flux is presented in Figures 4c (Simulation 1 with the deep learning model) and 4e (Simulation 2 with the statistical model). In this comparison, we focus on the storm main phase and early recovery phase when geomagnetic activity was most intense and dynamic, and structured precipitation patterns were evident. Different columns represent snapshots at different times, as marked in Figure 4a.

During the storm main phase (Times 1 and 2), POES observed strong precipitation on the dawn side (L > 3, 3-12 MLT) and enhanced precipitation at MLT~14, coinciding with the modeled plume region. Both simulations (Figures 4c and 4e) showed similar features, with strong chorus-induced precipitation on the dawn side and enhanced precipitation within the plume due to hiss. Note that during the storm main phase, POES was subject to proton contamination, thus the observation on the night side was challenging to interpret. During the recovery phase from Time 3 to 6, POES observed strong precipitation at 03-12 MLT, which decreased quickly over time, suggesting weakening of chorus waves. Interestingly, within the modeled plume region on the dusk side, POES first observed weak precipitation and then intense precipitation (L=4-6.5) within 2 hours. This feature moved to later MLTs at Times 5 and 6, suggesting corotation with the Earth. The location of intense precipitation aligned well with the modeled plasmapause. Simulation 1 predicted the same precipitation evolution, with strong chorus-induced precipitation on the dawn side until the end of the storm main phase, and intensified plume hiss waves driving distinct precipitation that corotated with the Earth before dissipating. In contrast, Simulation 2 captured similar precipitation flux levels during the storm main phase but did not resolve the spatial patterns driven by individual waves, particularly the evolution of plume hiss waves. The electron precipitation evolution from observations and simulations during the entire period is shown in Movie S1 in the Supporting Information.

The absolute precipitating flux values differ between simulation and observation due to several reasons: (1) MEPED telescopes have a limited field of view and nonuniform angular response, thus do not capture the precipitating flux in the entire loss cone (Selesnick et al., 2020); (2) the differential flux observed by RBSP does not have sufficient pitch angle resolution to measure the trapped flux, thus overestimates the induced precipitation (Castillo et al., 2024); (3) potential bias may be present in estimating chorus and hiss wave intensity due to their highly imbalanced dataset (Chu et al., 2023). (4) the whistler-mode wave models and parameters may have uncertainties compared to those during a specific event, including the wave normal angle distribution, wave power distribution along the field line, and wave frequency spectrum. Nevertheless, the precipitation dynamics induced by hiss and chorus waves agree very well both spatially and temporally, allowing us to draw conclusions on the relative contribution of whistler mode waves to electron precipitation on a global scale.

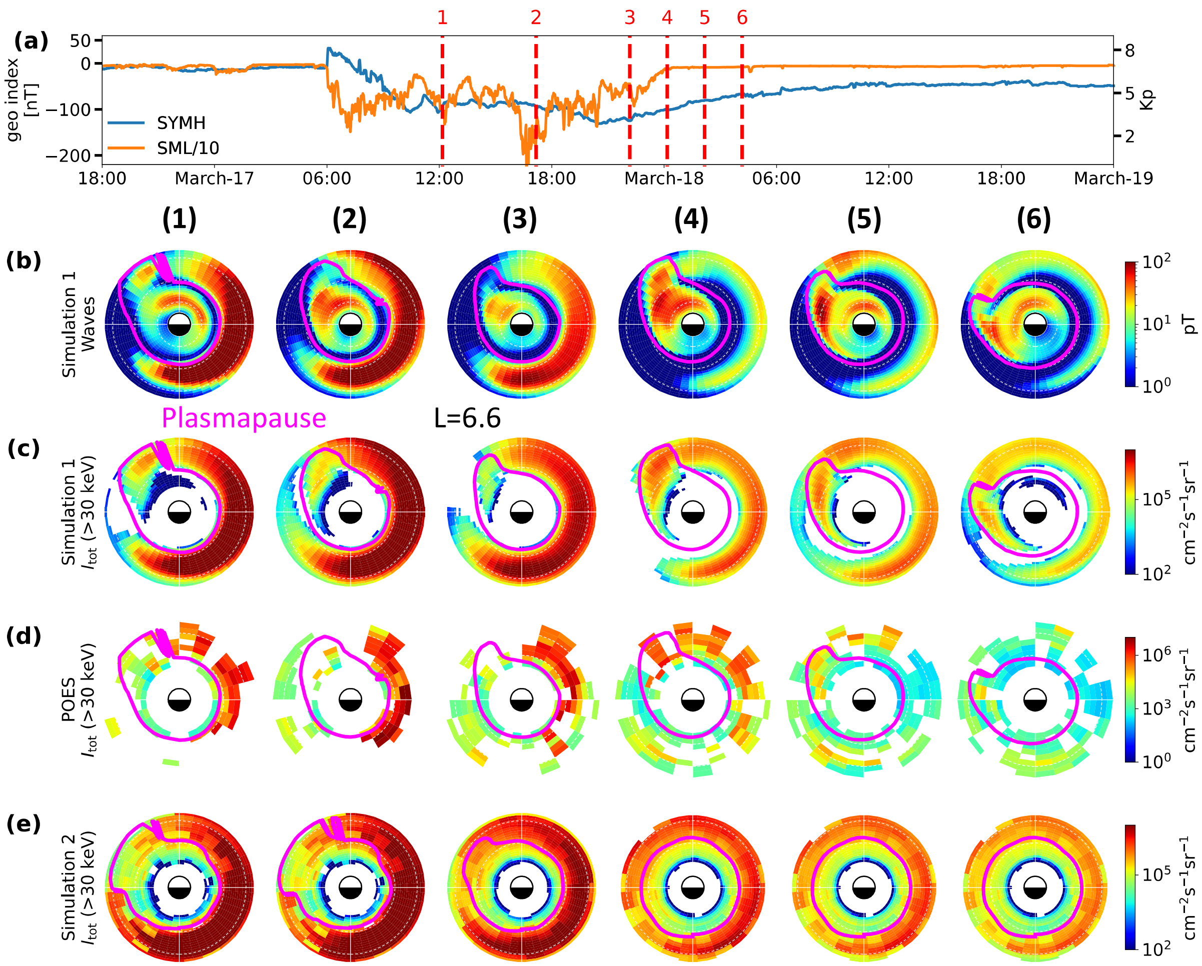

Figure 4. Comparison of simulated and observed precipitating electron fluxes. (a) Geomagnetic indices. (b) Whistler mode wave amplitudes modeled with neural networks at times marked in (a). The magenta line indicates the plasmapause location, separating hiss (inside) and chorus (outside). (c) Simulated precipitating electron flux using parameters from the deep learning approach. (d) Binned POES observations of precipitating electron flux at > 30 keV. (e) Simulated precipitating electron flux using statistical parameters.

5. Conclusions and Discussion

Understanding the complex dynamics of electron precipitation is challenging due to limited wave observations on a global scale. We performed a two-stage simulation to quantify the evolution of electron precipitation driven by whistler mode chorus and hiss waves. First, we modeled the global evolution of electron density, hiss and chorus wave amplitudes, and trapped electron flux using neural networks trained on RBSP observations. Then, based on quasi-linear theory, we computed the pitch angle scattering effect driven by the modeled whistler mode waves and calculated electron flux within the loss cone. We applied this simulation to the 17 March 2013 geomagnetic storm and compared results with the POES observations.

During the storm main phase, the simulated precipitating energy flux was an order of magnitude higher than during quiet times, mostly driven by chorus waves with peak energy flux of 20 erg/cm^2/s from the premidnight to noon sector, and characteristic energies ranging from 10 keV (early main phase) to 50 keV (later main phase). Hiss-driven precipitation was most significant in the plume region during the recovery phase, with energy flux up to 3 erg/cm^2/s, comparable to or even slightly stronger than chorus-driven precipitation. The characteristic energy of hiss-driven precipitation varied from 10 keV ($L > 6$ in the early main phase) to 200 keV ($L \sim 3.5$ in the recovery phase). The simulation using statistical density and wave parameters showed similar precipitation levels when averaged over time. However, it exhibited less dynamics compared to the modeling results using neural networks, since the statistical distribution of wave activity could not adequately capture the temporal and spatial evolution of waves after the storm main phase where the whole plasmasphere and associated waves were actively evolving.

Comparing simulation results with the POES observations, we found remarkable correlations: 1. strong precipitation driven by chorus waves over 03-12 MLT throughout the storm main phase, gradually decaying in the recovery phase; 2. isolated precipitation within the plasmaspheric plume in the storm main phase, with a burst at the start of the recovery phase; 3. regions of strong precipitation rotating with the Earth for hours, residing just inside the modeled plasmapause, suggesting plume hiss as its dominant driver.

With a 2-hour time resolution, our simulation demonstrates that, for this specific event, the electron precipitation observed by POES from the midnight to the afternoon sector can be primarily explained by the scattering effect of whistler mode chorus and hiss waves. This study quantifies the relative contribution of each wave mode at different storm phases, with chorus waves dominating throughout the storm main phase over 21-12 MLT, and plume hiss playing a key role in scattering electrons from 10 keV to 200 keV on the dusk side, particularly in the recovery phase. It is noteworthy that the conclusions drawn in this study are specific to this particular storm event and may not be applicable to other events in general. Further validation with additional data and case studies is necessary to draw broader conclusions. Nonetheless, this study provides an example of how to combine deep learning models with physics-based models to reproduce complex nonlinear systems and wave-particle interaction physics. The integration of more complex simulations and a comprehensive analysis of additional events will be pursued in the future.

Data Availability Statement

The Van Allen Probes data from the EMFISIS instrument (Kletzing et al., 2013) were accessed via the University of Iowa's EMFISIS website (VAP, 2013a). Data from the ECT instrument suite (Spence et al., 2013) were retrieved from the public archive hosted by the New Mexico Consortium (VAP, 2013b). The POES/MetOp satellite data were obtained from NOAA's National Centers for Environmental Information (POES, 2012). Geomagnetic indices used in model training, including SYM-H, were accessed from NASA's OMNIWeb (Papitashvili et al., 2020). The SML and SMU indices (Newell and Gjerloev, 2011) were accessed through the SuperMAG service (Gjerloev, 2012), and the Hp30 index (Matzka et al., 2022) was obtained from the GFZ Potsdam archive. All data used to produce figures are publicly available at https://doi.org/10.6084/m9.figshare.25612809.

Acknowledgments

SH gratefully acknowledges the NASA FINESST grant 80NSSC21K1385. WL, XS, QM, and LC acknowledge NASA grants 80NSSC24K0266, 80NSSC24K0239, 80NSSC21K1312, 80NSSC20K0196, 80NSSC24K0572, 80NSSC23K1054, and 80NSSC20K0704, as well as the NSF grant AGS-1847818, AGS-2225445, AGS-2247774, AGS-2402179, and AGS-2247265. XC would like to thank grant NASA ECIP 80NSSC19K0911, 80NSSC20K0196, 80NSSC22K1023, 80NSSC20K1325, 80NSSC23K0096, 80NSSC18K1227, NSF grant AGS-2247255, and AFOSR YIP FA9550-23-1-0359. We gratefully acknowledge the Van Allen Probes Mission, POES program, SuperMAG collaborators, GFZ collaborators and PyTorch team.

References

Abel, B., & Thorne, R. M. (1998). Electron scattering loss in Earth's inner magnetosphere: 1. Dominant physical processes. Journal of Geophysical Research: Space Physics, 103(A2), 2385–2396. https://doi.org/10.1029/97JA02919

Baker, D. N., Jaynes, A. N., Li, X., Henderson, M. G., Kanekal, S. G., Reeves, G. D., et al. (2014). Gradual diffusion and punctuated phase space density enhancements of highly relativistic electrons: Van Allen Probes observations. Geophysical Research Letters, 41(5), 1351–1358. https://doi.org/10.1002/2013GL058942

Blake, J. B., Carranza, P. A., Claudepierre, S. G., Clemmons, J. H., Crain, W. R., Dotan, Y., et al. (2013). The Magnetic Electron Ion Spectrometer (MagEIS) Instruments Aboard the Radiation Belt Storm Probes (RBSP) Spacecraft. Space Science Reviews, 179(1–4), 383–421. https://doi.org/10.1007/s11214-013-9991-8

Bortnik, J., Li, W., Thorne, R. M., & Angelopoulos, V. (2016). A unified approach to inner magnetospheric state prediction. Journal of Geophysical Research: Space Physics, 121(3), 2423–2430. https://doi.org/10.1002/2015JA021733

Bortnik, J., Chu, X., Ma, Q., Li, W., Zhang, X., Thorne, R. M., et al. (2018). Chapter 11 - Artificial Neural Networks for Determining Magnetospheric Conditions. In E. Camporeale, S. Wing, & J. R. Johnson (Eds.), Machine Learning Techniques for Space Weather (pp. 279–300). Elsevier. https://doi.org/10.1016/B978-0-12-811788-0.00011-1

Breneman, A. W., Halford, A., Millan, R., McCarthy, M., Fennell, J., Sample, J., et al. (2015). Global-scale coherence modulation of radiation-belt electron loss from plasmaspheric hiss. Nature, 523(7559), 193–195. https://doi.org/10.1038/nature14515

Capannolo, L., Li, W., Ma, Q., Shen, X. -C., Zhang, X. -J., Redmon, R. J., et al. (2019). Energetic Electron Precipitation: Multievent Analysis of Its Spatial Extent During EMIC Wave Activity. Journal of Geophysical Research: Space Physics, 124(4), 2466–2483. https://doi.org/10.1029/2018JA026291

Capannolo, L., Li, W., Spence, H., Johnson, A. T., Shumko, M., Sample, J., & Klumpar, D. (2021). Energetic Electron Precipitation Observed by FIREBIRD-II Potentially Driven by EMIC Waves: Location, Extent, and Energy Range From a Multievent Analysis.

Geophysical Research Letters, 48(5), e2020GL091564. https://doi.org/10.1029/2020GL091564

Capannolo, L., Li, W., & Huang, S. (2022). Identification and Classification of Relativistic Electron Precipitation at Earth Using Supervised Deep Learning. Frontiers in Astronomy and Space Sciences, 9. https://doi.org/10.3389/fspas.2022.858990

Castillo, A. M., Shprits, Y. Y., Aseev, N. A., Smirnov, A., Drozdov, A., Cervantes, S., et al. (2024). Can We Intercalibrate Satellite Measurements by Means of Data Assimilation? An Attempt on LEO Satellites. Space Weather, 22(1), e2023SW003624. https://doi.org/10.1029/2023SW003624

Chakraborty, S., Chakrabarty, D., Reeves, G. D., Baker, D. N., Claudepierre, S. G., Breneman, A. W., et al. (2021). Van Allen Probe Observations of Disappearance, Recovery and Patchiness of Plasmaspheric Hiss Following Two Consecutive Interplanetary Shocks: First Results. Journal of Geophysical Research: Space Physics, 126(4), e2020JA028873. https://doi.org/10.1029/2020JA028873

Chen, M. W., Lemon, C. L., Hecht, J., Sazykin, S., Wolf, R. A., Boyd, A., & Valek, P. (2019). Diffuse Auroral Electron and Ion Precipitation Effects on RCM-E Comparisons With Satellite Data During the 17 March 2013 Storm. Journal of Geophysical Research: Space Physics, 124(6), 4194–4216. https://doi.org/10.1029/2019JA026545

Chu, X., Bortnik, J., Li, W., Ma, Q., Angelopoulos, V., & Thorne, R. (2017a). Erosion and refilling of the plasmasphere during a geomagnetic storm modeled by a neural network. Journal of Geophysical Research: Space Physics, 122(7), 7118–7129.

Chu, X., Bortnik, J., Li, W., Ma, Q., Denton, R., Yue, C., et al. (2017b). A neural network model of three-dimensional dynamic electron density in the inner magnetosphere. Journal of Geophysical Research: Space Physics, 122(9), 9183–9197. https://doi.org/10.1002/2017JA024464

Chu, X., Ma, D., Bortnik, J., Tobiska, W. K., Cruz, A., Bouwer, S. D., et al. (2021). Relativistic Electron Model in the Outer Radiation Belt Using a Neural Network Approach. Space Weather, 19(12), e2021SW002808. https://doi.org/10.1029/2021SW002808

Chu, X., Bortnik, J., Li, W., Shen, X.-C., Ma, Q., Ma, D., et al. (2023). Distribution and Evolution of Chorus Waves Modeled by a Neural Network: The Importance of Imbalanced Regression. Space Weather, 21(10), e2023SW003524. https://doi.org/10.1029/2023SW003524

Chu, X., Bortnik, J., Shen, X.-C., Ma, Q., Li, W., Ma, D., et al. (2024). Imbalanced regressive neural network model for whistler-mode hiss waves: Spatial and temporal evolution. Journal of Geophysical Research: Space Physics, 129, e2024JA032761. https://doi.org/10.1029/2024JA032761

Clark, G., Tao, C., Mauk, B. H., Nichols, J., Saur, J., Bunce, E. J., et al. (2018). Precipitating Electron Energy Flux and Characteristic Energies in Jupiter's Main Auroral Region as Measured by Juno/JEDI. Journal of Geophysical Research: Space Physics, 123(9), 7554–7567. https://doi.org/10.1029/2018JA025639

Evans, D. S., & Greer, M. S. (2004). Polar Orbiting Environmental Satellite Space Environment Monitor - 2 Instrument Descriptions and Archive Data Documentation.

Fu, X., Cowee, M. M., Friedel, R. H., Funsten, H. O., Gary, S. P., Hospodarsky, G. B., et al. (2014). Whistler anisotropy instabilities as the source of banded chorus: Van Allen Probes observations and particle-in-cell simulations. Journal of Geophysical Research: Space Physics, 119(10), 8288–8298. https://doi.org/10.1002/2014JA020364

Funsten, H. O., Skoug, R. M., Guthrie, A. A., MacDonald, E. A., Baldonado, J. R., Harper, R. W., et al. (2013). Helium, Oxygen, Proton, and Electron (HOPE) Mass Spectrometer for the Radiation Belt Storm Probes Mission. Space Science Reviews, 179(1–4), 423–484. https://doi.org/10.1007/s11214-013-9968-7

Gjerloev, J. W. (2012), The SuperMAG data processing technique, J. Geophys. Res., 117, A09213, doi:10.1029/2012JA017683.

Green, J. C. (2013). MEPED Telescope Data Processing ALGORITHM THEORETICAL BASIS DOCUMENT.

Hikishima, M., Omura, Y., & Summers, D. (2010). Microburst precipitation of energetic electrons associated with chorus wave generation. Geophysical Research Letters, 37(7), 2010GL042678. https://doi.org/10.1029/2010GL042678

Hochreiter, S., & Schmidhuber, J. (1997). Long Short-Term Memory. Neural Computation, 9(8), 1735–1780. https://doi.org/10.1162/neco.1997.9.8.1735

Huang, S., Li, W., Shen, X.-C., Ma, Q., Chu, X., Ma, D., et al. (2022). Application of Recurrent Neural Network to Modeling Earth’s Global Electron Density. Journal of Geophysical Research: Space Physics, 127(9), e2022JA030695. https://doi.org/10.1029/2022JA030695

Huang, S., Li, W., Ma, Q., Shen, X. -C., Capannolo, L., Hanzelka, M., et al. (2023). Deep learning model of hiss waves in the plasmasphere and plumes and their effects on radiation belt electrons. Frontiers in Astronomy and Space Sciences, 10, 1231578. https://doi.org/10.3389/fspas.2023.1231578

Kasahara, S., Miyoshi, Y., Yokota, S., Mitani, T., Kasahara, Y., Matsuda, S., et al. (2018). Pulsating aurora from electron scattering by chorus waves. Nature, 554(7692), 337–340. https://doi.org/10.1038/nature25505

Kletzing, C. A., Kurth, W. S., Acuna, M., MacDowall, R. J., Torbert, R. B., Averkamp, T., et al. (2013). The Electric and Magnetic Field Instrument Suite and Integrated Science (EMFISIS) on RBSP. Space Science Reviews, 179(1–4), 127–181. https://doi.org/10.1007/s11214-013-9993-6

Kurth, W. S., De Pascuale, S., Faden, J. B., Kletzing, C. A., Hospodarsky, G. B., Thaller, S., & Wygant, J. R. (2015). Electron densities inferred from plasma wave spectra obtained by the Waves instrument on Van Allen Probes. Journal of Geophysical Research: Space Physics, 120(2), 904–914. https://doi.org/10.1002/2014JA020857

Lam, M. M., Horne, R. B., Meredith, N. P., & Glauert, S. A. (2007). Modeling the effects of radial diffusion and plasmaspheric hiss on outer radiation belt electrons. Geophysical Research Letters, 34(20), L20112. https://doi.org/10.1029/2007GL031598

Lam, Mai Mai, Horne, R. B., Meredith, N. P., Glauert, S. A., Moffat-Griffin, T., & Green, J. C. (2010). Origin of energetic electron precipitation >30 keV into the atmosphere. Journal of Geophysical Research: Space Physics, 115(A4), 2009JA014619. https://doi.org/10.1029/2009JA014619

Li, W., Thorne, R. M., Meredith, N. P., Horne, R. B., Bortnik, J., Shprits, Y. Y., & Ni, B. (2008). Evaluation of whistler mode chorus amplification during an injection event observed on CRRES. Journal of Geophysical Research: Space Physics, 113(A9), 2008JA013129. https://doi.org/10.1029/2008JA013129

Li, W., Thorne, R. M., Angelopoulos, V., Bortnik, J., Cully, C. M., Ni, B., et al. (2009). Global distribution of whistler-mode chorus waves observed on the THEMIS spacecraft. Geophysical Research Letters, 36(9), 2009GL037595. https://doi.org/10.1029/2009GL037595

Li, W., Bortnik, J., Thorne, R. M., & Angelopoulos, V. (2011). Global distribution of wave amplitudes and wave normal angles of chorus waves using THEMIS wave observations: CHORUS WAVE DISTRIBUTION ON THEMIS. Journal of Geophysical Research: Space Physics, 116(A12), n/a-n/a. https://doi.org/10.1029/2011JA017035

Li, W., Thorne, R. M., Ma, Q., Ni, B., Bortnik, J., Baker, D. N., et al. (2014). Radiation belt electron acceleration by chorus waves during the 17 March 2013 storm. Journal of Geophysical Research: Space Physics, 119(6), 4681–4693. https://doi.org/10.1002/2014JA019945

Li, W., Ma, Q., Thorne, R. M., Bortnik, J., Kletzing, C. A., Kurth, W. S., et al. (2015). Statistical properties of plasmaspheric hiss derived from Van Allen Probes data and their effects on radiation belt electron dynamics. Journal of Geophysical Research: Space Physics, 120(5), 3393–3405. https://doi.org/10.1002/2015JA021048

Li, W., Santolik, O., Bortnik, J., Thorne, R. M., Kletzing, C. A., Kurth, W. S., & Hospodarsky, G. B. (2016). New chorus wave properties near the equator from Van Allen Probes wave observations. Geophysical Research Letters, 43(10), 4725–4735. https://doi.org/10.1002/2016GL068780

Li, W., Shen, X. -C., Ma, Q., Capannolo, L., Shi, R., Redmon, R. J., et al. (2019). Quantification of Energetic Electron Precipitation Driven by Plume Whistler Mode Waves, Plasmaspheric Hiss, and Exohiss. Geophysical Research Letters, 46(7), 3615–3624. https://doi.org/10.1029/2019GL082095

Lyons, L. R., Gallardo-Lacourt, B., Zou, S., Weygand, J. M., Nishimura, Y., Li, W., et al. (2016). The 17 March 2013 storm: Synergy of observations related to electric field modes and their ionospheric and magnetospheric Effects. Journal of Geophysical Research: Space Physics, 121(11). https://doi.org/10.1002/2016JA023237

Lyons, Lawrence R., Thorne, R. M., & Kennel, C. F. (1972). Pitch-angle diffusion of radiation belt electrons within the plasmasphere. Journal of Geophysical Research, 77(19), 3455–3474. https://doi.org/10.1029/JA077i019p03455

Ma, D., Bortnik, J., Ma, Q., Hua, M., & Chu, X. (2023, July 14). Machine Learning Interpretability of Outer Radiation Belt Enhancement \& Depletion Events. arXiv. https://doi.org/10.48550/arXiv.2307.09192

Ma, D., Bortnik, J., Ma, Q., Hua, M., & Chu, X. (2024). Machine Learning Interpretability of Outer Radiation Belt Enhancement and Depletion Events. Geophysical Research Letters, 51(1), e2023GL106049. https://doi.org/10.1029/2023GL106049

Ma, Q., Ni, B., Tao, X., & Thorne, R. M. (2012). Evolution of the plasma sheet electron pitch angle distribution by whistler-mode chorus waves in non-dipole magnetic fields. Annales Geophysicae, 30(4), 751–760. https://doi.org/10.5194/angeo-30-751-2012

Ma, Q., Li, W., Thorne, R. M., Ni, B., Kletzing, C. A., Kurth, W. S., et al. (2015). Modeling inward diffusion and slow decay of energetic electrons in the Earth's outer radiation belt. Geophysical Research Letters, 42(4), 987–995. https://doi.org/10.1002/2014GL062977

Ma, Q., Li, W., Thorne, R. M., Bortnik, J., Reeves, G. D., Kletzing, C. A., et al. (2016). Characteristic energy range of electron scattering due to plasmaspheric hiss. Journal of Geophysical Research: Space Physics, 121(12). https://doi.org/10.1002/2016JA023311

Ma, Q., W. Li, J. Bortnik, R. M. Thorne, X. Chu, L. G. Ozeke, G. D. Reeves, C. A. Kletzing, W. S. Kurth, G. B. Hospodarsky, M. J. Engebretson, H. E. Spence, D. N. Baker, J. B. Blake, J. F. Fennell, and S. G. Claudepierre (2018), Quantitative evaluation of radial diffusion and local acceleration processes during GEM challenge events, Journal of Geophysical Research: Space Physics, 123, 1938–1952, doi:10.1002/2017JA025114.

Ma, Q., Connor, H. K., Zhang, X. -J., Li, W., Shen, X. -C., Gillespie, D., et al. (2020). Global Survey of Plasma Sheet Electron Precipitation due to Whistler Mode Chorus Waves in Earth's Magnetosphere. Geophysical Research Letters, 47(15), e2020GL088798. https://doi.org/10.1029/2020GL088798

Ma, Q., Li, W., Zhang, X. -J., Bortnik, J., Shen, X. -C., Connor, H. K., et al. (2021). Global Survey of Electron Precipitation due to Hiss Waves in the Earth's Plasmasphere and Plumes. Journal of Geophysical Research: Space Physics, 126(8), e2021JA029644. https://doi.org/10.1029/2021JA029644

Ma, Qianli, Chu, X., Ma, D., Huang, S., Li, W., Bortnik, J., & Shen, X.-C. (2023). Evaluating the performance of empirical models of total electron density and whistler-mode wave amplitude in the Earth's inner magnetosphere. Frontiers in Astronomy and Space Sciences, 10. https://doi.org/10.3389/fspas.2023.1232702

Matzka, Jürgen; Bronkalla, Oliver; Kervalishvili, Guram; Rauberg, Jan; Yamazaki, Yosuke (2022): Geomagnetic Hpo index. V. 2.0. GFZ Data Services. https://doi.org/10.5880/Hpo.0002

Mauk, B. H., Fox, N. J., Kanekal, S. G., Kessel, R. L., Sibeck, D. G., & Ukhorskiy, A. (2013). Science Objectives and Rationale for the Radiation Belt Storm Probes Mission. Space Science Reviews, 179(1–4), 3–27. https://doi.org/10.1007/s11214-012-9908-y

Meredith, N. P., Horne, R. B., Sicard-Piet, A., Boscher, D., Yearby, K. H., Li, W., & Thorne, R. M. (2012). Global model of lower band and upper band chorus from multiple satellite observations. Journal of Geophysical Research: Space Physics, 117(A10), 2012JA017978. https://doi.org/10.1029/2012JA017978

Meredith, N. P., Horne, R. B., Glauert, S. A., Thorne, R. M., Summers, D., Albert, J. M., & Anderson, R. R. (2006). Energetic outer zone electron loss timescales during low geomagnetic activity. *Journal of Geophysical Research: Space Physics*, *111*(A5), 2005JA011516. https://doi.org/10.1029/2005JA011516

Meredith, N. P., Horne, R. B., & Anderson, R. R. (2001). Substorm dependence of chorus amplitudes: Implications for the acceleration of electrons to relativistic energies. *Journal of Geophysical Research: Space Physics*, *106*(A7), 13165–13178. https://doi.org/10.1029/2000JA900156

Meredith, N. P., Horne, R. B., Glauert, S. A., & Anderson, R. R. (2007). Slot region electron loss timescales due to plasmaspheric hiss and lightning-generated whistlers: SLOT REGION ELECTRON LOSS TIMESCALES. Journal of Geophysical Research: Space Physics, 112(A8), n/a-n/a. https://doi.org/10.1029/2007JA012413

Meredith, N. P., Horne, R. B., Glauert, S. A., Baker, D. N., Kanekal, S. G., & Albert, J. M. (2009). Relativistic electron loss timescales in the slot region. Journal of Geophysical Research: Space Physics, 114(A3), 2008JA013889. https://doi.org/10.1029/2008JA013889

Millan, R. M., & Thorne, R. M. (2007). Review of radiation belt relativistic electron losses. Journal of Atmospheric and Solar-Terrestrial Physics, 69(3), 362–377. https://doi.org/10.1016/j.jastp.2006.06.019

Newell, P. T., and J. W. Gjerloev (2011), Evaluation of SuperMAG auroral electrojet indices as indicators of substorms and auroral power, J. Geophys. Res., 116, A12211, doi:10.1029/2011JA016779.

Ni, B., Thorne, R. M., Shprits, Y. Y., & Bortnik, J. (2008). Resonant scattering of plasma sheet electrons by whistler-mode chorus: Contribution to diffuse auroral precipitation. Geophysical Research Letters, 35(11), L11106. https://doi.org/10.1029/2008GL034032

Ni, B., Bortnik, J., Thorne, R. M., Ma, Q., & Chen, L. (2013). Resonant scattering and resultant pitch angle evolution of relativistic electrons by plasmaspheric hiss. Journal of Geophysical Research: Space Physics, 118(12), 7740–7751. https://doi.org/10.1002/2013JA019260

Ni, B., Bortnik, J., Nishimura, Y., Thorne, R. M., Li, W., Angelopoulos, V., et al. (2014). Chorus wave scattering responsible for the Earth's dayside diffuse auroral precipitation: A detailed case study. Journal of Geophysical Research: Space Physics, 119(2), 897–908. https://doi.org/10.1002/2013JA019507

Nishimura, Y., Bortnik, J., Li, W., Thorne, R. M., Lyons, L. R., Angelopoulos, V., et al. (2010). Identifying the Driver of Pulsating Aurora. Science, 330(6000), 81–84. https://doi.org/10.1126/science.1193186

Nishimura, Y., Bortnik, J., Li, W., Thorne, R. M., Ni, B., Lyons, L. R., et al. (2013). Structures of dayside whistler-mode waves deduced from conjugate diffuse aurora. Journal of Geophysical Research: Space Physics, 118(2), 664–673. https://doi.org/10.1029/2012JA018242

Papitashvili, Natalia E. and King, Joseph H. (2020). OMNI 1-min Data [Dataset]. NASA Space Physics Data Facility. https://doi.org/10.48322/45bb-8792

Peck, E. D., Randall, C. E., Green, J. C., Rodriguez, J. V., & Rodger, C. J. (2015). POES MEPED differential flux retrievals and electron channel contamination correction. Journal of Geophysical Research: Space Physics, 120(6), 4596–4612. https://doi.org/10.1002/2014JA020817

Pettit, J. M., Randall, C. E., Peck, E. D., & Harvey, V. L. (2021). A New MEPED-Based Precipitating Electron Data Set. Journal of Geophysical Research: Space Physics, 126(12), e2021JA029667. https://doi.org/10.1029/2021JA029667

POES. (2012). Electron precipitation by Medium Energy Proton and Electron Detector (MEPED) instruments [Dataset]. Polar Orbiting Environmental Satellites (POES) Space Environment Monitor (SEM). https://www.ngdc.noaa.gov/stp/satellite/poes/dataaccess.html

Qin, M., Li, W., Ma, Q., Woodger, L., Millan, R., Shen, X., & Capannolo, L. (2021). Multi-Point Observations of Modulated Whistler-Mode Waves and Energetic Electron Precipitation. Journal of Geophysical Research: Space Physics, 126(12), e2021JA029505. https://doi.org/10.1029/2021JA029505

Reidy, J. A., Horne, R. B., Glauert, S. A., Clilverd, M. A., Meredith, N. P., Woodfield, E. E., et al. (2021). Comparing Electron Precipitation Fluxes Calculated From Pitch Angle Diffusion Coefficients to LEO Satellite Observations. Journal of Geophysical Research: Space Physics, 126(3), e2020JA028410. https://doi.org/10.1029/2020JA028410

Rodger, C. J., Clilverd, M. A., Green, J. C., & Lam, M. M. (2010). Use of POES SEM-2 observations to examine radiation belt dynamics and energetic electron precipitation into the atmosphere. Journal of Geophysical Research: Space Physics, 115(A4), 2008JA014023. https://doi.org/10.1029/2008JA014023

Schunk, R. W., Scherliess, L., Eccles, V., Gardner, L. C., Sojka, J. J., Zhu, L., et al. (2021). Challenges in Specifying and Predicting Space Weather. Space Weather, 19(2), e2019SW002404. https://doi.org/10.1029/2019SW002404

Selesnick, R. S., Tu, W., Yando, K., Millan, R. M., & Redmon, R. J. (2020). POES/MEPED Angular Response Functions and the Precipitating Radiation Belt Electron Flux. Journal of Geophysical Research: Space Physics, 125(9), e2020JA028240. https://doi.org/10.1029/2020JA028240

Shen, X., Li, W., Ma, Q., Agapitov, O., & Nishimura, Y. (2019). Statistical Analysis of Transverse Size of Lower Band Chorus Waves Using Simultaneous Multisatellite Observations. Geophysical Research Letters, 46(11), 5725–5734. https://doi.org/10.1029/2019GL083118

Shen, X., Li, W., Capannolo, L., Ma, Q., Qin, M., Artemyev, A. V., et al. (2023). Modulation of Energetic Electron Precipitation Driven by Three Types of Whistler Mode Waves. Geophysical Research Letters, 50(8), e2022GL101682. https://doi.org/10.1029/2022GL101682

Søraas, F., Sandanger, M. I., & Smith-Johnsen, C. (2018). NOAA POES and MetOp particle observations during the 17 March 2013 storm. Journal of Atmospheric and Solar-Terrestrial Physics, 177, 115–124. https://doi.org/10.1016/j.jastp.2017.09.004

Spence, H. E., Reeves, G. D., Baker, D. N., Blake, J. B., Bolton, M., Bourdarie, S., et al. (2013). Science Goals and Overview of the Radiation Belt Storm Probes (RBSP) Energetic Particle, Composition, and Thermal Plasma (ECT) Suite on NASA's Van Allen Probes Mission. Space Science Reviews, 179(1–4), 311–336. https://doi.org/10.1007/s11214-013-0007-5

Stix, T. H. (1992). Waves in plasmas.

Su, Z., Zhu, H., Xiao, F., Zheng, H., Wang, Y., He, Z., et al. (2014). Intense duskside lower band chorus waves observed by Van Allen Probes: Generation and potential acceleration effect on radiation belt electrons. Journal of Geophysical Research: Space Physics, 119(6), 4266–4273. https://doi.org/10.1002/2014JA019919

Thorne, R. M., Ni, B., Tao, X., Horne, R. B., & Meredith, N. P. (2010). Scattering by chorus waves as the dominant cause of diffuse auroral precipitation. Nature, 467(7318), 943–946. https://doi.org/10.1038/nature09467

Thorne, R. M., Bortnik, J., Li, W., & Ma, Q. (2021). Wave–Particle Interactions in the Earth's Magnetosphere. In R. Maggiolo, N. André, H. Hasegawa, D. T. Welling, Y. Zhang, & L. J. Paxton (Eds.), Geophysical Monograph Series (1st ed., pp. 93–108). Wiley. https://doi.org/10.1002/9781119815624.ch6

VAP. (2013a). The Electric and Magnetic Field Instrument Suite and Integrated Science (EMFISIS) [Dataset]. Van Allen Probes Mission (VAP). http://emfisis.physics.uiowa.edu/Flight/

VAP. (2013b). Energetic Particle, Composition, and Thermal Plasma (ECT) Suite [Dataset]. Van Allen Probes Mission (VAP). https://rbsp-ect.newmexicoconsortium.org/data_pub/

Walton, S. D., Forsyth, C., Rae, I. J., Meredith, N. P., Sandhu, J. K., Walach, M. -T., & Murphy, K. R. (2022). Statistical Comparison of Electron Loss and Enhancement in the Outer Radiation Belt During Storms. Journal of Geophysical Research: Space Physics, 127(5), e2021JA030069. https://doi.org/10.1029/2021JA030069

Wang, W., Huang, Y., Wang, Y., & Wang, L. (2014). Generalized Autoencoder: A Neural Network Framework for Dimensionality Reduction. In 2014 IEEE Conference on

Computer Vision and Pattern Recognition Workshops (pp. 496–503). Columbus, OH, USA: IEEE. https://doi.org/10.1109/CVPRW.2014.79

Xiao, F., Yang, C., He, Z., Su, Z., Zhou, Q., He, Y., et al. (2014). Chorus acceleration of radiation belt relativistic electrons during March 2013 geomagnetic storm. Journal of Geophysical Research: Space Physics, 119(5), 3325–3332. https://doi.org/10.1002/2014JA019822

Yando, K., Millan, R. M., Green, J. C., & Evans, D. S. (2011). A Monte Carlo simulation of the NOAA POES Medium Energy Proton and Electron Detector instrument: TECHNIQUE. Journal of Geophysical Research: Space Physics, 116(A10), n/a-n/a. https://doi.org/10.1029/2011JA016671

Zhelavskaya, I. S., Shprits, Y. Y., & Spasojević, M. (2017). Empirical Modeling of the Plasmasphere Dynamics Using Neural Networks. Journal of Geophysical Research: Space Physics, 122(11), 11,227-11,244. https://doi.org/10.1002/2017JA024406

Zhu, H., Shprits, Y. Y., Chen, L., Liu, X., & Kellerman, A. C. (2018). An Event on Simultaneous Amplification of Exohiss and Chorus Waves Associated With Electron Density Enhancements. Journal of Geophysical Research: Space Physics, 123(11), 8958–8968. https://doi.org/10.1029/2017JA025023

Figure 1.

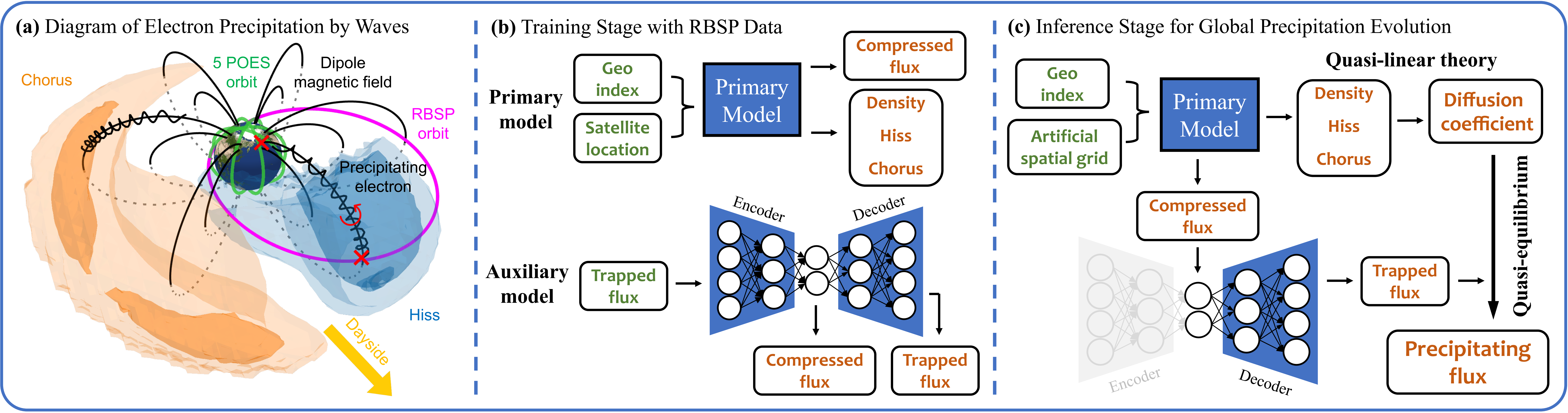

(a) Diagram of Electron Precipitation by Waves
Chorus
5 POES orbit
Dipole magnetic field
RBSP orbit
Precipitating electron
Hiss
Dayside
(b) Training Stage with RBSP Data
Primary model
Geo index
Satellite location
Primary Model
Compressed flux
Density
Hiss
Chorus
Auxiliary model
Trapped flux
Encoder
Decoder
Compressed flux
Trapped flux
(c) Inference Stage for Global Precipitation Evolution
Quasi-linear theory
Geo index
Artificial spatial grid
Primary Model
Density
Hiss
Chorus
Diffusion coefficient
Compressed flux
Quasi-equilibrium
Encoder
Decoder
Trapped flux
Precipitating flux

Figure 2.

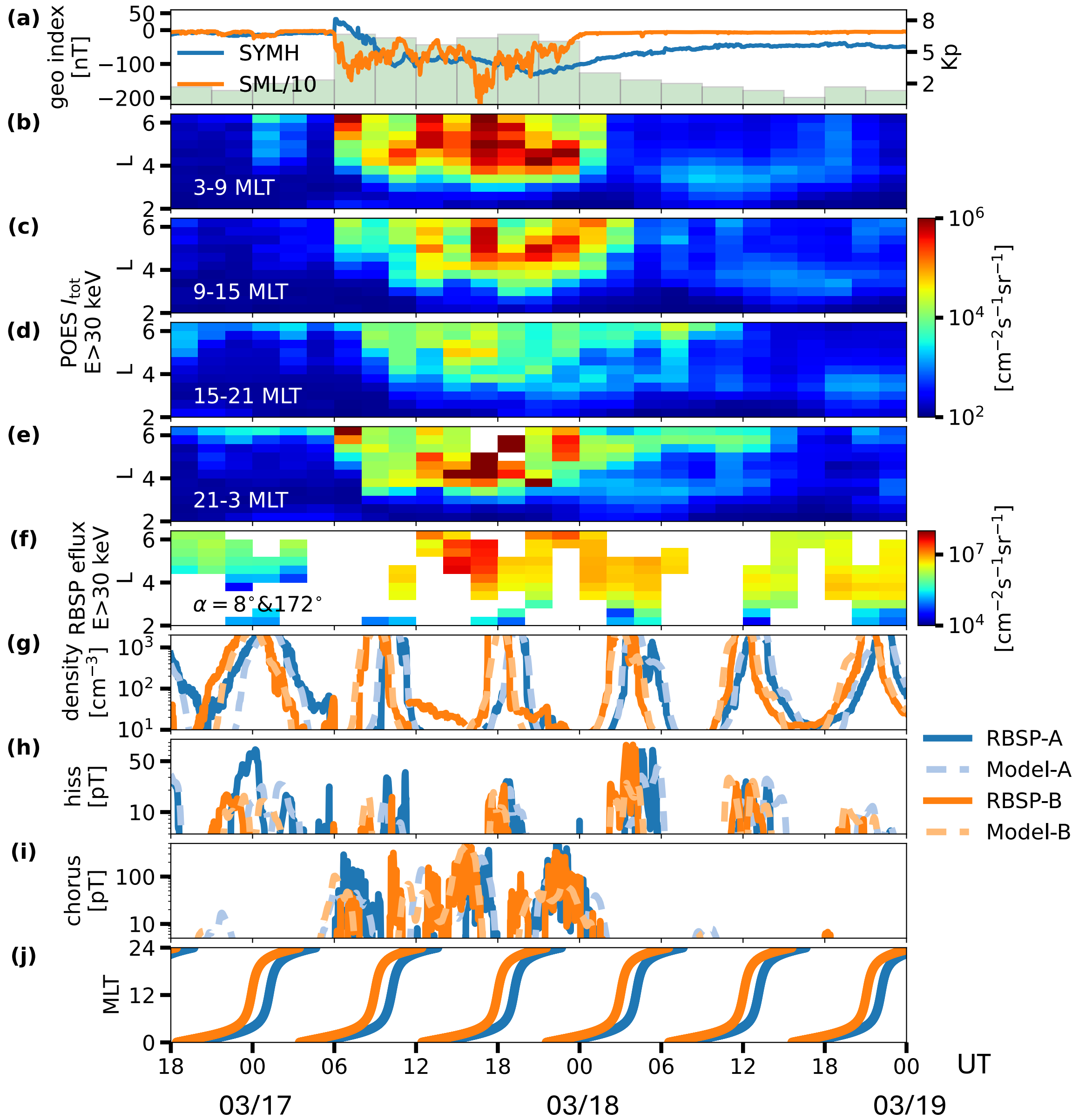
(a)
geo index [nT]
SYMH
SML/10
Kp
(b)
3-9 MLT
(c)
9-15 MLT
(d)
15-21 MLT
(e)
21-3 MLT
POES I_{tot} E>30 keV
[cm^{-2}s^{-1}sr^{-1}]
(f)
RBSP eflux E>30 keV
$\alpha = 8°\&172°$
(g)
density [cm^{-3}]
(h)
hiss [pT]
(i)
chorus [pT]
(j)
MLT
RBSP-A
Model-A
RBSP-B
Model-B
UT
03/17
03/18
03/19

Figure 3.

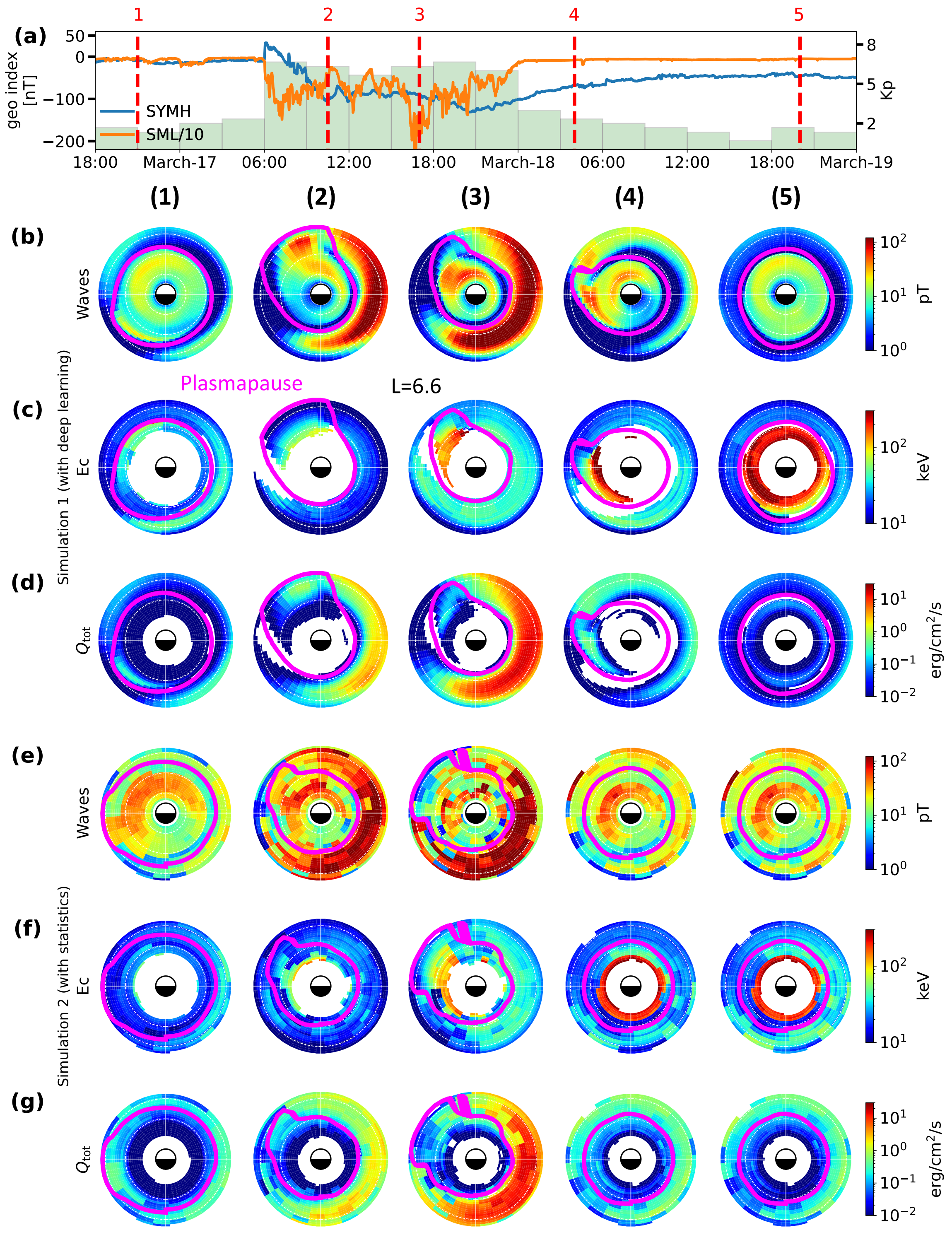

1
2
3
4
5
(a)
geo index [nT]
Kp
SYMH
SML/10
18:00
March-17
06:00
12:00
18:00
March-18
06:00
12:00
18:00
March-19
(1)
(2)
(3)
(4)
(5)
(b)
Waves
pT
Plasmapause
L=6.6
(c)
Ec
keV
Simulation 1 (with deep learning)
(d)
Q_{tot}
erg/cm^2/s
(e)
Waves
pT
(f)
Ec
keV
Simulation 2 (with statistics)
(g)
Q_{tot}
erg/cm^2/s

Figure 4.

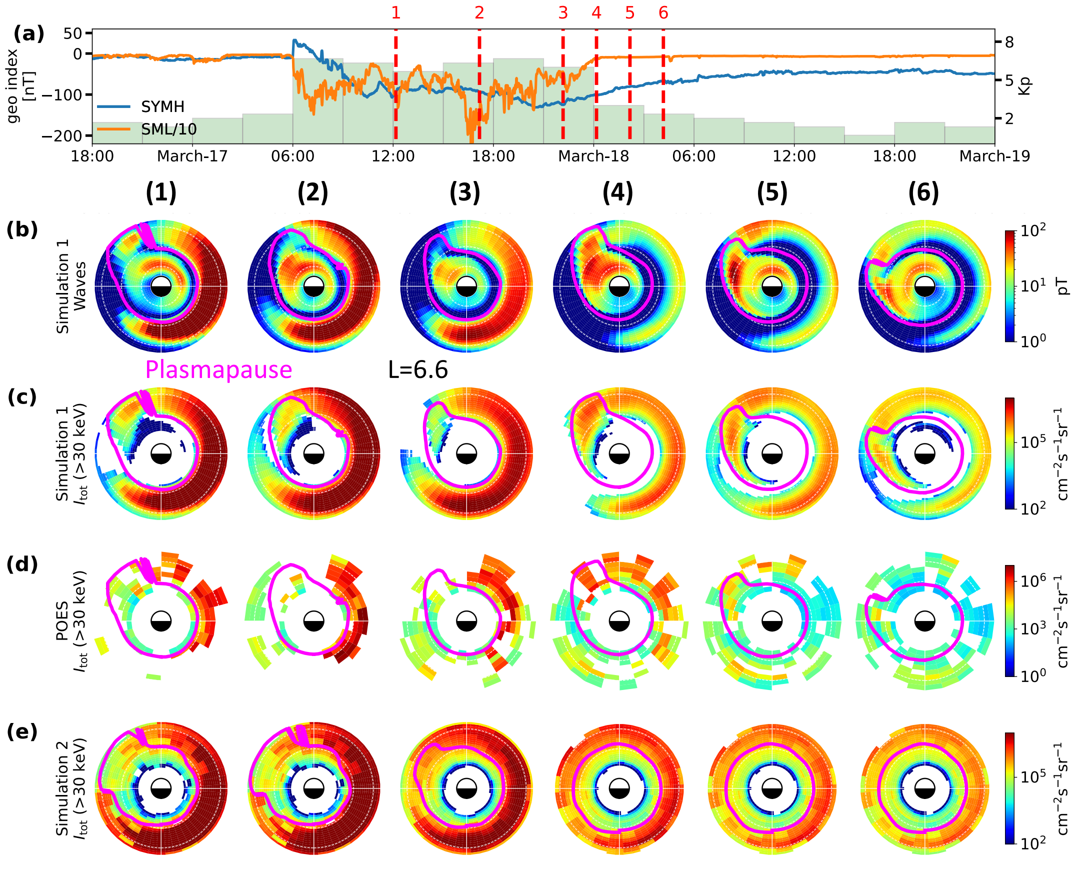

(a)
1
2
3
4
5
6
geo index [nT]
50
0
−100
−200
SYMH
SML/10
Kp
8
5
2
18:00
March-17
06:00
12:00
18:00
March-18
06:00
12:00
18:00
March-19
(1)
(2)
(3)
(4)
(5)
(6)
(b)
Simulation 1 Waves
10^2
10^1
10^0
pT
Plasmapause
L=6.6
(c)
Simulation 1 I_{tot} (>30 keV)
10^5
10^2
$cm^{-2}s^{-1}sr^{-1}$
(d)
POES I_{tot} (>30 keV)
10^6
10^3
10^0
$cm^{-2}s^{-1}sr^{-1}$
(e)
Simulation 2 I_{tot} (>30 keV)
10^5
10^2
$cm^{-2}s^{-1}sr^{-1}$